Article

Not peer-reviewed version

Toward Carbon-Negative Construction Materials: CO_2-Storing Alkali-Activated Waste-Based Binder

Aleksandar Nikolov * , Nadia Petrova , Miryana Raykovska , Ivan Georgiev , Alexander Karamanov

Posted Date: 14 February 2026

doi: 10.20944/preprints202602.1097.v1

Keywords: alkali-activated materials; carbonation curing; CO2-storage; CO2 sequestration; carbon-negative; ladle furnace slag; cement kiln dust; coal ash; γ-belite doi:10.20944/preprints202602.1097.v1

Article

Toward Carbon-Negative Construction Materials: CO_2-Storing Alkali-Activated Waste-Based Binder

Aleksandar Nikolov [1,*], Nadia Petrova [1,2], Miryana Raykovska [3], Ivan Georgiev [3] and Alexander Karamanov [4]

[1] Institute of Mineralogy and Crystallography, Bulgarian Academy of Sciences, IMC-BAS, Acad. G. Bonchev Str., bl. 107, 1113 Sofia, Bulgaria
[1] Center for Competence - PERIMED-2, Central District, Vasil Aprilov Blvd. 15A, 4002 Plovdiv, Bulgaria
[3] Institute of Information and communication technology, Bulgarian Academy of Sciences, Acad. G. Bonchev Str., bl. 2, 1113 Sofia, Bulgaria
[4] Institute for Physical Chemistry, Bulgarian Academy of Sciences, IPC-BAS, Bl. 11, Acad. G. Bonchev Str., 1113-Sofia, Bulgaria
* Correspondence: drsashko@imc.bas.bg

Abstract

This study examines the carbonation behavior and CO_2 storage potential of a Ca-rich alkali-activated binder produced entirely from industrial residues, namely ladle furnace slag (LFS), coal ash (CA), and cement kiln dust (CKD). The system was designed as a one-part alkali-activated material (AAM), with CKD acting as an internal activator, and subjected to ambient curing, water curing, and accelerated CO_2 curing at ambient pressure. Phase evolution, microstructural development, and pore-structure characteristics were investigated using X-ray diffraction, FTIR spectroscopy, DSC–TG analysis, scanning electron microscopy, and X-ray micro-computed tomography, together with measurements of density, water absorption, and compressive strength. CO_2 curing fundamentally altered the reaction pathway of the binder, shifting it from hydration-dominated to carbonation-controlled phase evolution, leading to the decomposition of calcium-bearing hydrates and complete carbonation of non-hydraulic γ-belite with the formation of vaterite, aragonite, and calcite. These transformations induced pronounced microstructural densification, reflected in a near-doubling of compressive strength (>48 MPa), increased apparent density, reduced water absorption, and simplified pore-network topology. The results demonstrate that controlled carbonation is an effective post-treatment strategy for waste-derived alkali-activated binders, enabling simultaneous performance enhancement and permanent CO_2 sequestration.

Keywords: alkali-activated materials; carbonation curing; CO_2-storage; CO_2 sequestration; carbon-negative; ladle furnace slag; cement kiln dust; coal ash; γ-belite

1. Introduction

The construction and operation of buildings are the highest contributor of global CO_2 emissions, accounting for 34 per cent of total emissions [1]. The building material production is dominated by the most used building material Portland cement which alone accounts for approximately 7–8% of global anthropogenic CO_2 emissions. Despite continuous improvements in energy efficiency and clinker substitution, conventional decarbonization pathways remain insufficient to meet the climate targets defined by international frameworks [2]. Recent comprehensive reviews have demonstrated that achieving net-zero or near-zero emissions in cement and concrete production requires the integration of disruptive technologies, including alternative binders, carbon capture, and in-material CO_2 utilization [3–5]. In this context, the paradigm is shifting from merely reducing emissions toward actively transforming construction materials into carbon sinks, enabling the emergence of carbon-negative building systems.

Carbon capture and utilization strategies in cementitious materials have gained significant scientific and industrial attention, particularly through mineral carbonation [4,6]. The mineral carbonation exploit the reactivity of alkaline and alkaline-earth phases toward CO_2, forming thermodynamically stable carbonates that permanently bind carbon [7]. One of the approaches is the production of carbonated fillers or aggregates using waste materials such as concrete waste powder [8–10], steel slag [11], olivine [12], cement kiln dust [13,14], biomass ash [15] , fly ash, calcium carbide sludge [16], etc. This strategy enables the incorporation of CO_2 storage into both conventional and alternative concrete systems, since aggregates constitute a substantial volumetric fraction of concrete and therefore represent an effective and scalable sink for mineralized carbon. Other approach is to obtain binders that hardens through carbonation.

Carbonation curing of cementitious materials involves early-age treatment in a sealed chamber under a normal or pressurized, high-concentration CO_2 atmosphere [17]. This approach can be applied even to ordinary Portland cement systems, where CO_2 reacts with calcium silicate phases to form a hybrid binder matrix composed of calcium–silicate–hydrate (C–S–H) and calcium carbonate ($CaCO_3$)[18]. Nevertheless, the intrinsic decarbonation of limestone step associated with Portland cement production can only be partially mitigated by such a carbonation strategy.

In contrast, AAMs are generally produced without the need of decarbonation of raw materials and typically rely on industrial by-products, resulting in substantially lower CO_2 emissions [19]. Moreover, alkali-activated materials contain high concentrations of alkali and alkaline-earth elements, making them particularly promising candidates for effective carbon curing and CO_2 capture [20,21]. Recent experimental studies demonstrate that waste-based alkali-activated composites can achieve meaningful compressive strengths while storing measurable quantities of CO_2 under ambient conditions, without the need for energy-intensive curing regimes [22]. Ladle furnace slag (LFS) and cement kiln dust (CKD) has emerged as a particularly promising precursors for alkali-activated materials with high potential for CO_2 capture [14,23–25]. The presence of reactive Ca-bearing phases enables both alkali activation and subsequent mineral carbonation, positioning LFS and CKD as a suitable candidates for carbon-storing binder systems.

In our recent work, LFS was shown to be effectively activated using CKD as a solid alkali source, enabling the development of one-part alkali-activated binders without the need for external liquid alkali activators [26]. An optimal addition of 20 wt.% CKD to LFS-CA blend was identified, resulting in the highest mechanical performance under ambient curing conditions. This finding demonstrates that CKD can simultaneously function as an internal activator and a calcium source, enhancing both early reactivity and structural development.

This study explores carbonation behaviors of the one-part alkali activated cement comprised exclusively of industrial residues—ladle furnace slag, cement kiln dust, and coal ash. The results provide new insights into the potential of waste-derived AAMs to act as CO_2 sinks, while simultaneously transforming waste streams and by-products into valuable construction materials.

2. Materials and Methods

The precursors of the alkali-activated material investigated in this study were ladle furnace slag (LFS), coal ash (CA), and cement kiln dust (CKD). The LFS was collected from an outside stockpile located in the yard of a steel plant, provided by Aeiforos Bulgaria S.A. The CA originated from the Maritsa Iztok-2 thermal power plant, which operates on lignite coal. The CA represents a composite waste stream comprising fly ash, bottom ash, and flue gas desulfurization by-products, all of which are hydraulically transported and deposited mixed in an ash pond [27]. Prior to use, the LFS and CA were oven-dried at 80 °C to constant mass and subsequently ground separately in a ball mill for 1 h to ensure fineness and reactivity similar to cement. CKD, supplied by Heidelberg Materials Devnya JSC, was used as a dry alkali activator without additional processing (CKD-2 at [28]). Based on our previous work [26]], the optimal composition of the three precursors was determined as LSF:CA:CKD = 75:25:20 (wt.%). The corresponding chemical composition was calculated accordingly and is presented in Table 1.

Table 1. Chemical composition of the precursors and calculated composition of the binder blend used at the presented study.

	Na_2O	MgO	Al_2O_3	SiO_2	SO_3	Cl	K_2O	CaO	TiO_2	MnO	Fe_2O_3	Others
LFS[1]	-	6.50	15.50	15.60	2.45	-	0.10	55.50	0.70	0.80	2.69	0.16
CA[1]	0.74	1.87	15.02	29.75	17.61	-	1.11	18.20	0.52	0.08	14.84	0.26
CKD[1]	1.51	0.47	1.79	5.39	4.39	11.81	16.65	55.51	0.17	0.03	1.59	0.69
LFS/CA/CKD[2] – 75/25/20	0.41	4.53	13.12	16.85	5.93	1.97	3.07	47.73	0.57	0.52	5.04	0.27

[1] The chemical composition determined by wave-dispersive XRF in our previous study [26] [2] Calculated chemical composition based on [1].

The powder X-ray diffractograms were obtained on Empyrean (Malvern Panalytical, Malvern, UK) diffractometer using CuKα radiation at 40 kV and 30 mA. Infrared spectra were recorded with a Fourier transform infrared spectrometer, Tensor 37 spectrometer (Bruker, Berlin, Germany) in the mid infrared range 4000 – 400 cm^{-1}, using a 13 mm in diameter KBr pellets. The thermal behavior of the compounds was studied using DSC-TG analyzer Setsys Evolution2400 (SETARAM, France) on 10 mg of the sample in static air atmosphere with heating rate of 10° C min^{-1} from room temperature to 1000° C. The SEM images were obtained on a JEOL 6390 apparatus (Jeol USA, Inc., Peabody, MA, USA) at 20 kV under a secondary electron regime. The observed specimen was a fracture piece prepared with gold cover under vacuum. The Micro-CT scanning was conducted using a Nikon XT H 225 micro-computed tomography system, providing a resolution of 15 microns with a continuous 360° rotation, 120kV/ 150μA. A total of 2880 images were acquired during each scan with exposure time of 500ms. Reconstruction of the tomographic data was carried out using Nikon Metrology's CT Pro-3D software, and porosity analysis was subsequently performed with VG STUDIO MAX (version 2023.4.), with a pore size threshold of 15 μm.

The absolute density was measured using a gas pycnometer (AccyPy1330, Micromeritic, Norcross, GA, USA) on a grinded in agate mortar samples. The apparent density was determined using hydrostatic weighing method. Water absorption was calculated based on dry mass and the mass of the watered to constant mass specimens. Relative density was calculated based on apparent and absolute densities. Compressive strength was determined using three cubic specimens with a loading face area of 10 cm^2 each series. The carbonation depth experiments were performed on fresh split specimens using a standard indicator solution of phenolphthalein (1 g phenolphthalein dissolved in 70 ml ethyl alcohol and diluted to 100 ml with distilled water).

The accelerated aging was performed at atmospheric pressure in plastic box filled with CO_2 gas. Chamber with the samples was wrapped in polyethylene foil in order to prevent CO_2 leakage. Carbon dioxide gas (≥99%) was injected periodically with opened exit valve on the top of the lid. Optimal conditions for carbonation (65% relative humidity) were maintained using saturated ammonium nitrate solution (wt. 50%) at the bottom of the box.

3. Results

3.1. Specimen Preparation and Curing Conditions

Our previous experiments showed the optimal recipe LF20 - 750 grams of LFS, 250 g CA and 200 g CKD [26]. The ingredients were dry pre-mixed in a planetary mixer, then water was added at water to solid ratio equal of 0.34. The fresh mixtures were cast into steel molds, sealed with polyethylene foil, and stored under laboratory conditions for 24 h. After one day, the specimens were demolded and transferred to different curing regimes. Series LF20 was placed in laboratory conditions (20 °C, 50% relative humidity), series LF20-W was placed in container filled with tap water; LF20-C - in carbonation chamber (20 °C, 65% relative humidity, 99% CO_2). The specimens were cured in these conditions a day prior the 28^{-th} day, were prepared for the testing.

3.2. Carbonation Depth—Phenolphthalein Test

Three cubes from each series were split and sprayed with phenolphthalein indicator solution at 28^{-th} day to visualize the depth of CO_2 penetration (Figure 1). The specimens cured under water (LF20-W) showed almost no carbonation, indicated by a uniform pink color across the split surface. The LF20 series, cured under laboratory air, exhibited an approximately 5 mm outer layer where CO_2 ingress had neutralized the high pH, as evidenced by the loss of pink coloration. Specimens cured in the carbonation chamber (LF20-C) displayed complete CO_2 penetration. Interesting to note was that series LF20-W showed darker inner zone immediately after splitting, which gradually turned to gray after 10–15 minutes. This phenomenon is likely related to a phase change upon contact with atmospheric CO_2.

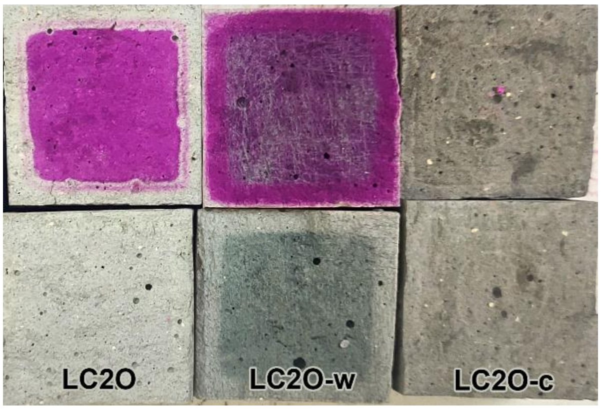

Figure 1. Phenolphthalein test performed in freshly split cubes shows pink zones with pH above 10.

3.3. Physical Properties

The results indicate that water curing (LF20-W) does not significantly affect the physical properties compared with ambient laboratory curing (LF20) (Table 2). In contrast, the carbonated series (LF20-C) exhibits pronounced changes in physical performance, with compressive strength increased almost twice and exceeding 48 MPa. This strength gain correlates well with the observed increase in apparent density, indicating extensive densification of the material. At the same time, a significant reduction in relative porosity is observed, confirming the progressive filling and refinement of the pore structure. A slight decrease in absolute density is also detected, which can be interpreted as evidence for the formation of new phases. This transformation is accompanied by a pronounced reduction in water absorption after carbonation, reflecting the closure of capillary pores and the overall decrease in permeability.

Table 2. Compressive strength, density, and water absorption of the alkali-activated pastes under different curing conditions.

Series	Curing conditions	Compressive strength, MPa	Apparent density, g/cm³	Absolute density, g/cm³	Relative porosity, %	Water absorption, %
LF20	50% RH	25.2 ± 0.4	1.56	2.628	40.64	25.2 ± 0.2
LF20-W	Under water	25.7 ± 0.7	1.52	2.649	42.62	26.9 ± 0.2
LF20-C	65% RH, 99% CO_2	48.2 ± 0.7	1.74	2.552	31.82	17.9 ± 0.1

3.4. Powder XRD

The XRD patterns reveal significant differences in phase composition depending on the curing environment (Figure 2). The LF20 and LF20-W series—cured in ambient air and under water, respectively—exhibit broadly similar mineralogical profiles. In both cases, the dominant crystalline hydration products are AFt (ettringite) and AFm (hydrocalumite) phases. Their formation is consistent with the sulfate-rich chemistry of the CA and CKD components, and the presence of reactive alumina-bearing phases such as mayenite and gehlenite in the LFS. In series LF20-W the ettringite formation was higher compared to LF20, and margarite phase were detected. Margarite is calcium rich member of the mica group observed to crystalize in calcium-aluminate cements used in geothermal wells after prolonged water curing under water [29,30]. In LF20 and LF20-W, γ-belite and periclase largely remained unreacted.

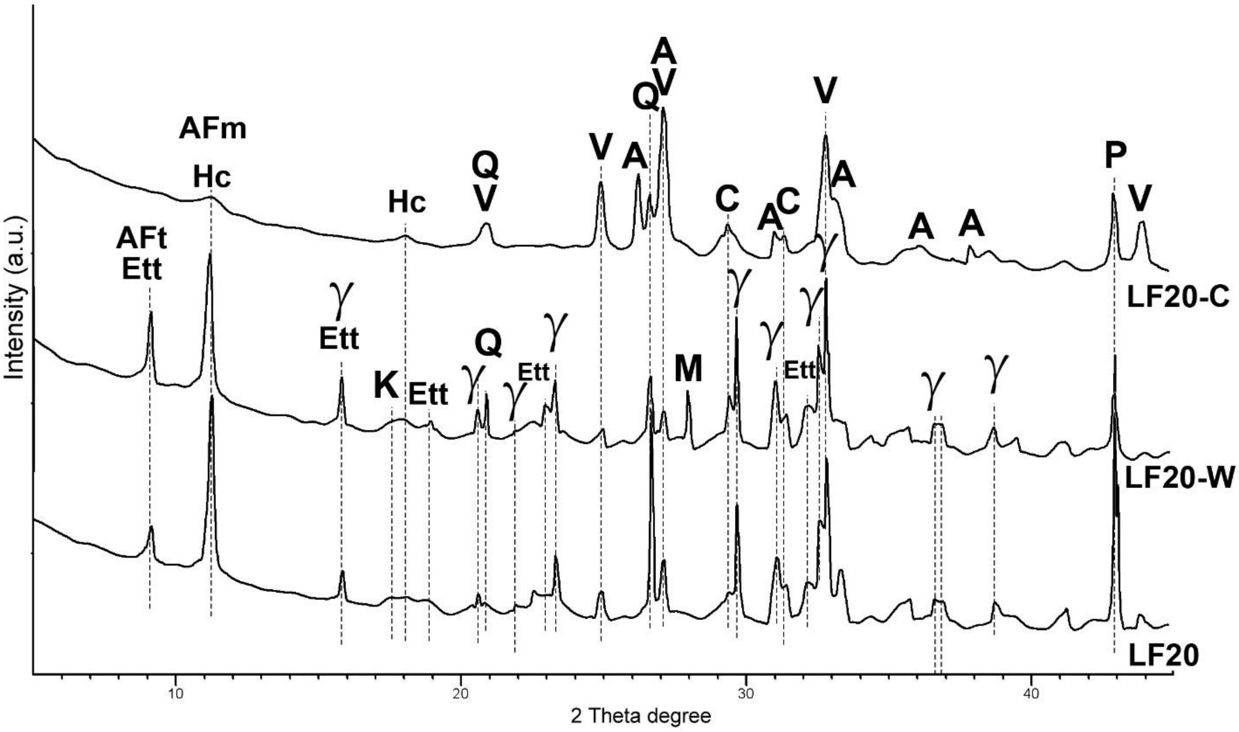

Figure 2. Powder XRD diffractograms of the alkali-activated pastes cured in different conditions. Legend: A – aragonite, $CaCO_3$; AFm- aluminate ferrite monosubstituted phases; Aft - aluminate ferrite trisubstituted phases; C - calcite, $CaCO_3$; Ett - ettringite, $Ca_6Al_2(SO_4)_3(OH)_{12}\cdot 26H_2O$; Hc - hydrocalumite, $Ca_2Al(OH)_{6.5}Cl_{0.5}.3(H_2O)$; M – margarite, $CaAl_2(Al_2Si_2O_{10})(OH)_2$; P - periclase, MgO; Q - quartz, SiO_2; V- vaterite, $CaCO_3$; γ - γ-belite (γ-C_2S/γ-Ca_2SiO_4).

On other hand, the carbonated series LF20-C was subjected to significant mineralogical alterations. The carbonation process triggered the complete decomposition of hydrated phases – ettringite and katoite, as well as near-total transformation of hydrocalumite. Moreover, the non-hydrated γ-belite, exhibited complete carbonation. This indicates that γ-belite undergo carbonation without the need of hydration. The products of carbonation were three polymorphs of calcium carbonate—vaterite, aragonite, and calcite. The simultaneous presence of these polymorphs suggests dynamic transformation processes. Carbonation of the system proceeds through a multistage decalcification pathway in which calcium is progressively leached and precipitated as $CaCO_3$ polymorphs, while the partially disintegrated gel reorganizes. This process ultimately converts Ca-bearing hydrates into carbonate minerals and leaves behind residual silica–alumina gels which are X-ray amorphous.

3.5. DSC/TG

The thermal behavior of the mineral compositions of the series under this study shows processes of dehydration, dehydroxylation and decarbonization (Figure 3 and Table 2). These processes are expressed by endothermic events on the DSC curve and associated with mass losses on the TG curve. The main hydrous minerals in the series are hydrocalumite (AFm) and ettringite (AFt) and both of them are known as layer double hydroxides. The dehydration and dehydroxylation processes of these compounds have been largely investigated using DSC-TG methods as different types of water and hydroxyl groups in their structures have been differentiated, gradually evolving during heating from room temperature to about 450 °C [31–34]. For both hydrocalumite and ettringite the dehydration processes (I) are related to the interlayer water release in the temperature interval 25-220 °C while the dehydroxylation ones are associated with the evolving of hydroxyl groups from the structural layer in the temperature interval 220-480 °C (Figure 3) It was found that the mass losses associated with remove of physical water processes are greatest in the case of series LF20-W compering to LF20 and LF20-C (Table 2).

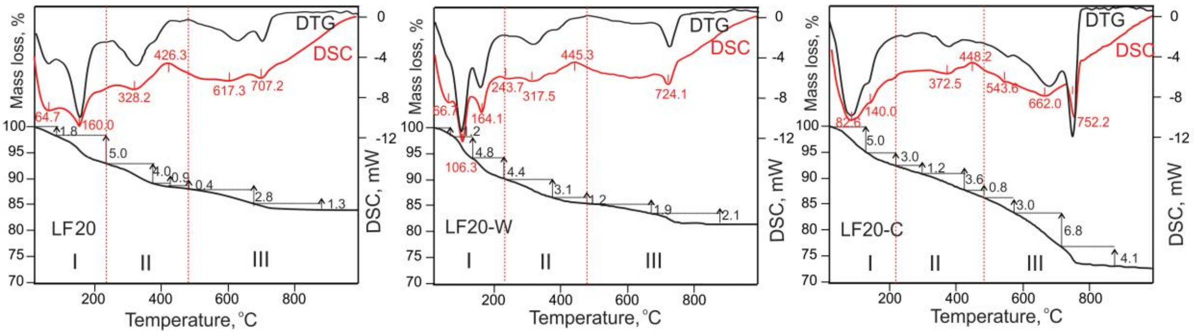

Figure 3. DSC/TG/DTG curves of the alkali-activated pastes cured in different conditions.

The thermal analysis revealed that all series exhibited endothermic peaks corresponding to carbonate decomposition, including the LF20-W series, which had been cured under water with no direct exposure to CO_2. This behavior may be attributed to natural carbonation or weathering of the LFS during outdoor storage. Among the series, LF20 displayed an intermediate carbonate content, whereas LF20-C exhibited markedly higher carbonate levels, as evidenced by the presence of two pronounced shoulder peaks at approximately 662 °C and 752 °C. The identified by XRD polymorph modifications of calcium carbonate minerals vaterite, aragonite, and calcite exhibit specific thermal behavior. The highly metastable vaterite transforms to calcite with a pronounced exothermic effect at temperatures 426 °C (LF20), 445 °C (LF20-W) and 448 °C (LF20-C). This type of transformation has been widely reported for both synthetic and natural materials. The corresponding temperature range is strongly influenced by the synthesis route in the case of synthetic samples and by the geological origin and structural characteristics of natural materials, and typically lies between approximately 420 °C and 515 °C [35,36]. Another metastable polymorph, thermodynamically more stable than vaterite, is aragonite, which undergoes transformation into calcite at elevated temperatures, typically above 550–600 °C [36]. This transformation is expressed in the case of LF20-C specimen, where an endothermic effect is observed at about 545 °C. The thermal decomposition temperature of calcite in the investigated series is approximately 50–70 °C lower than the values typically reported in the literature. A similar phenomenon has been observed for so-called “weathered calcite,” which is characterized by pronounced structural disorder, reduced thermal stability, and altered mass-loss behavior, often manifested as earlier onset, broadened, or multi-stage decomposition events [37]. Moreover, it was found that calcium carbonate decompose in alkaline media at lower temperature [38].

The TG results showed that LF20-C series contains a substantially higher amount of carbonate phases compared to the other two series, as evidenced by its several-fold greater mass loss during the decarbonation process, which also contributes to increased total mass loss (Table 2). These findings confirm extensive CO_2 penetration in the specimens cured within the carbonation chamber (LF20-C).

Table 2. Mass loss of the alkali-activated pastes during dehydration, dehydroxylation, and decarbonation under different curing conditions.

Series	(I)Dehydration-(II)Dehydroxylation, Mass, % (related mineral phases)	(III)Decarbonization Mass, % (related mineral phases)	Total Loss Mass, %
LF20	**12.1** (AFm, AFt)	**4.1** (vaterite, aragonite, calcite)	**16.2**
LF20-W	**14.7** (AFm, AFt, margarite)	**4.0** (vaterite, aragonite, calcite)	**18.7**
LF20-C	**13.6** (AFm, AFt)	**13.9** (vaterite, aragonite, calcite)	**27.5**

3.6. FTIR

The FTIR spectra of the samples provide insights into the structural changes induced by different curing conditions. The broad band observed at 3440–3450 cm^{-1} corresponds to the stretching vibrations of water molecules (–OH) (Figure 4). A shoulder at about 3638 cm^{-1}, present in the LF20 and LF20-W series, is attributed to the –OH stretching of the $Al(OH)_6$ units in ettringite or hydrocalumite [39,40]. In the high CO_2 environment, the decomposition of ettringite and most of the hydrocalumite leads to the disappearance of these bands in the LF20-C series.

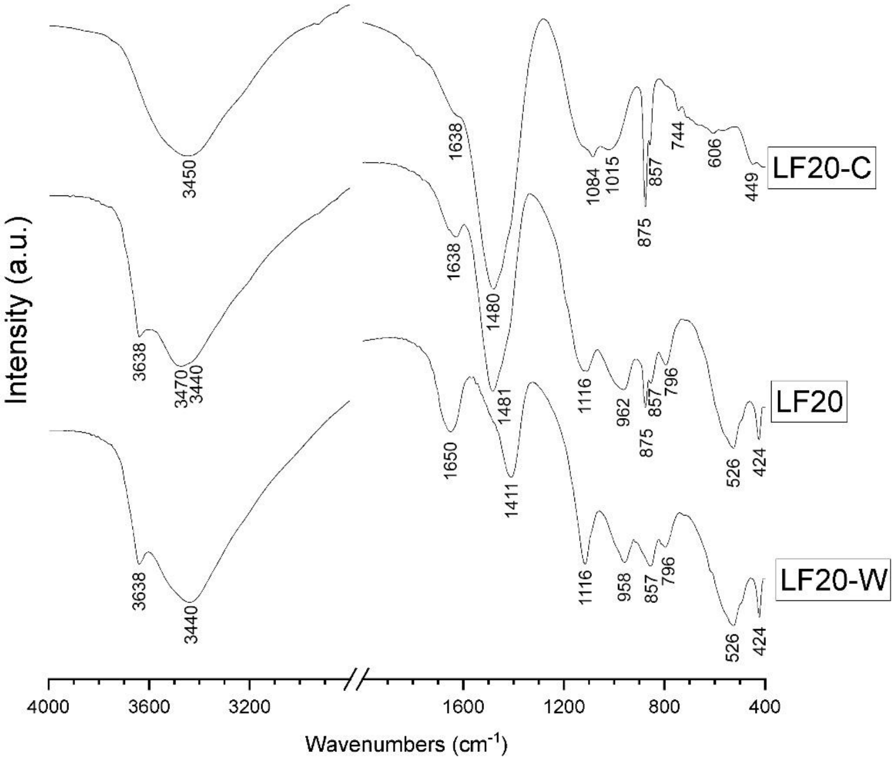

Figure 4. FTIR spectrums of the alkali-activated paste cured at different conditions.

The band at about 1411 cm^{-1} corresponds to the asymmetric stretching (ν_3) of CO_3^{2-}, likely arising from the carbonation of raw materials due to weathering during storage and natural adsorption of CO_2. While this band is clearly present in LF20-W, it also appears as a small shoulder in LF20 and LF20-C, adjacent to a more prominent new band at 1480–1481 cm^{-1}. The latter is assigned to the ν_3 mode of carbonate species and is characteristic of amorphous calcite, aragonite, and vaterite [41]. This band dominates the spectrum of LF20-C, reflecting extensive carbonation. A sharp band at approximately 875 cm⁻¹, corresponding to the ν2 vibration mode of CO_3^{2-}, is present in LF20 and becomes much more pronounced in LF20-C, indicating a substantial increase in carbonate content.

Sulfate-related band at 1116 cm⁻¹ (ν3 SO_4^{2-}) are evident in LF20 and LF20-W but significantly suppressed in the carbonated LF20-C sample, indicating the decomposition of sulfate-containing phases. The bands at 958–962 cm⁻¹ and 426 cm⁻¹ correspond to AlO_6 vibrations, while 857 cm⁻¹ Al–O–H deformations related to ettringite [41]. After carbonation curing the band at about 962 cm⁻¹ broadened and shifted 1015 cm⁻¹ which could be related to increased polymerization of the tetrahedral network, commonly associated with cation depletion, reduced non-bridging oxygens, and evolution toward a silica- and alumina-rich, more connected amorphous structure [42]. The small band about 1084 cm⁻¹ could be related to amorphous $Al(OH)_3$ [43].

Overall, the FTIR results demonstrate that curing conditions strongly influence the phase composition and chemical structure of the alkali-activated materials. The substantially increased intensity of the ν3 and ν2 carbonate bands confirms that carbonates are the dominant phases in LF20-C. These findings align with XRD and thermal analysis results, highlighting the synergistic effect of curing environment on phase transformations and the progressive incorporation of CO_2 into the material.

3.7. SEM

The SEM observations revealed notable differences in microstructure among the series (Figure 5). The LF20 and LF20-W samples exhibited similar microstructural features, characterized by the presence of needle-like crystals indicative of ettringite or hydrocalumite formation. In LF20, small microcracks were observed, likely resulting from drying shrinkage during the initial curing period, whereas LF20-W displayed a more uniform and compact structure, suggesting that water curing mitigated shrinkage-induced defects. In contrast, the LF20-C series exhibited a markedly different morphology. The microstructure of LF20-C was dominated by a pronounced globular texture, reflecting extensive carbonation and the formation of carbonate phases that modified the binder matrix. This globular morphology is consistent with the transformation of ettringite and hydrocalumite into calcium carbonate phases, as also evidenced by FTIR, XRD, and thermal analysis, and highlights the significant impact of CO_2 exposure on both the chemical composition and physical microstructure of the alkali-activated material.

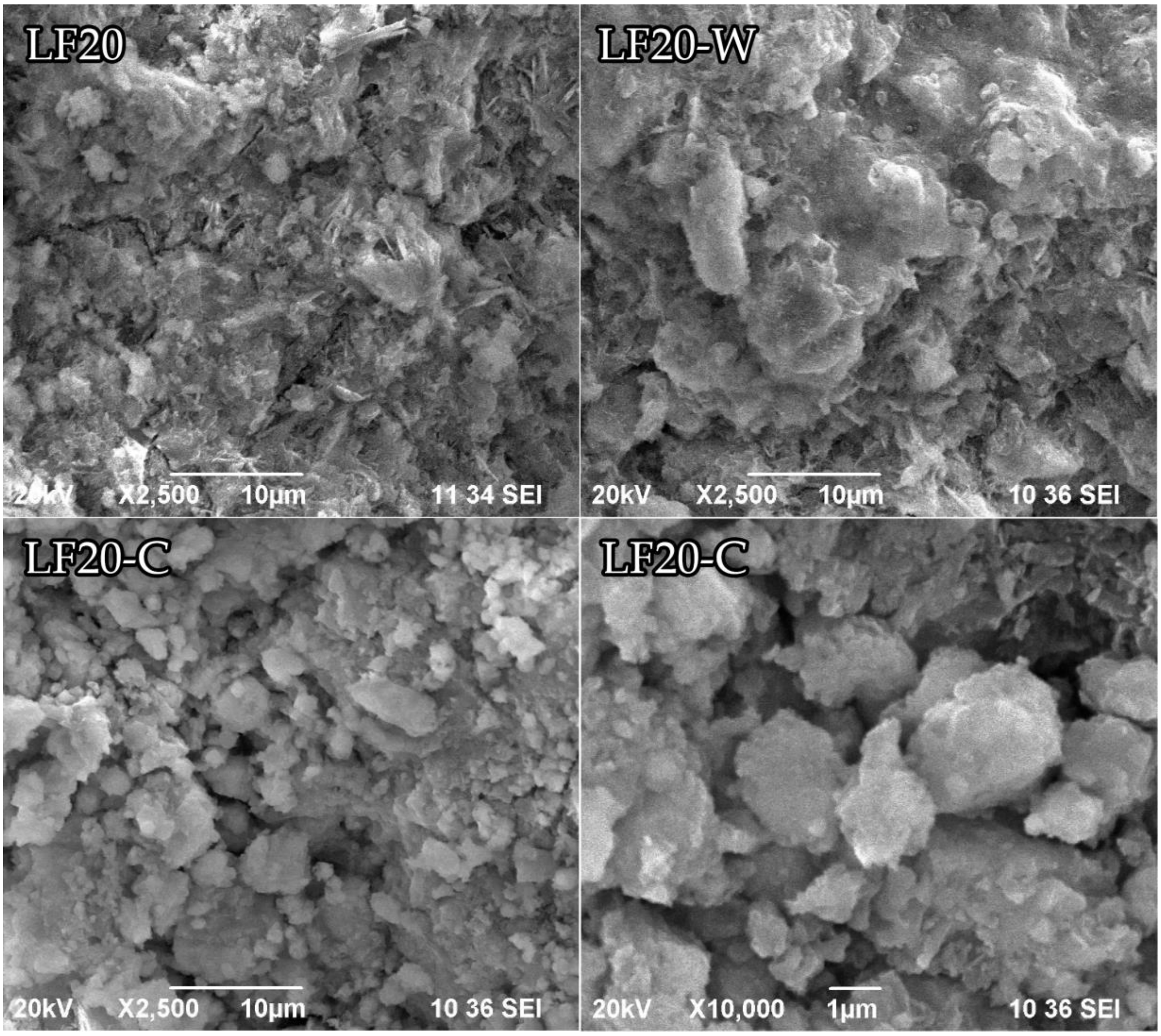

Figure 5. SEM images of alkali-activated pastes cured in different conditions.

3.8. X-Ray Computed Tomography (Micro-CT)

Micro-CT porosity analysis, applying a pore size threshold of 15 μm, revealed relatively narrow variations in total porosity among the investigated materials, ranging from 0.83% to 1.16%. To better capture differences in internal structure beyond porosity alone, the pore-specific surface area normalized by material volume (PSA/MV) was used together with the indication volume, representing the total segmented pore volume within the analyzed region. PSA/MV varied substantially from 0.590 to 0.895, indicating pronounced differences in pore morphology and internal surface complexity.

Material LF20-C exhibited the lowest total porosity, the lowest indication volume (274.26 mm^3), and the lowest PSA/MV value, reflecting a more compact and geometrically simplified pore structure. In contrast, materials LF 20-W and LF20 showed higher indication volumes (355.97 and 372.34 mm^3, respectively) and elevated PSA/MV values, representing a more irregular and structurally complex pore network. The comparison between LF20 and LF 20-W suggests a pore-refinement mechanism, in which a reduction in total pore volume is accompanied by increased surface complexity, consistent with a transition from a coarser pore network to a more refined, tortuous internal structure.

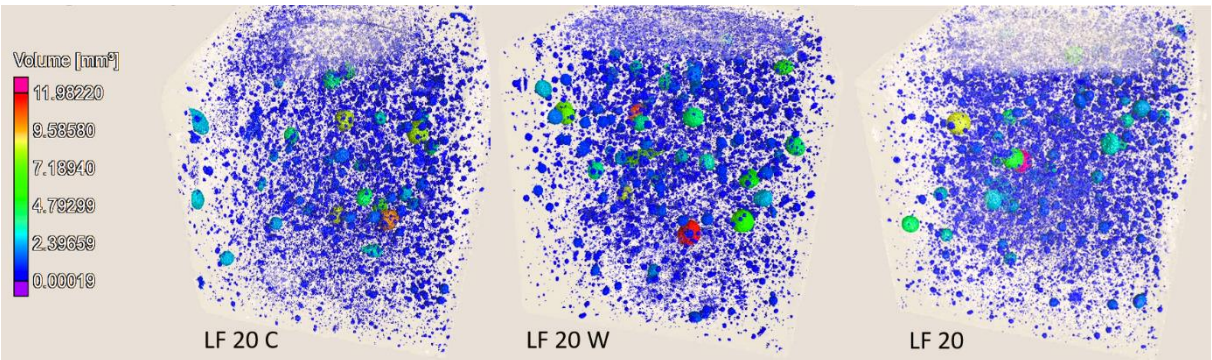

Figure 6. Three-dimensional micro-CT renderings of segmented pores in the LF 20 C, LF 20 W, and LF 20 samples. Pores are color-coded according to their individual volume (mm³), illustrating the spatial distribution and size range of pores within each material.

Table 3. Summary of micro-CT–derived porosity parameters calculated using a pore size threshold of 15 μm, corresponding to the spatial resolution of the measurement.

Series	Porosity (%)	PSA/MV	Indication volume (mm³)
LF20	1.16	0.855	372.34
LF20-W	1.09	0.895	355.97
LF20-C	0.83	0.590	274.26

4. Discussion

4.1. Carbonation as Mechanism of Strength Development

The results clearly demonstrate that accelerated CO_2 curing fundamentally alters the reaction pathway of the LFS–CA–CKD alkali-activated system, shifting it from hydration-dominated to carbonation-dominated phase evolution. The high degree of carbonation of the LF20-C specimens, confirmed by phenolphthalein testing, XRD, FTIR, and thermal analysis, is directly associated with a near-doubling of compressive strength and a substantial reduction in water absorption. The decomposition of AFt and AFm phases and their replacement by calcium carbonate polymorphs results in a denser and mechanically more stable microstructure. The precipitation of these carbonate phases within pore spaces effectively compacts the binder matrix, explaining the strong correlation between increased apparent density and compressive strength observed for LF20-C. Similar behavior has been reported for Ca-rich alkali-activated slags and CKD-containing binders, where carbonation promotes pore filling and increases mechanical strength [44–46].

Pore-structure metrics, including surface area, morphology, and tortuosity, are general method of analyzing the porous media behavior, with micro-CT providing robust quantification that enables direct correlation of pore volume, size, and spatial distribution with mechanical performance [47]. The micro-CT analysis allows direct assessment of the geometric complexity of the pore network, capturing features such as surface roughness, connectivity, and internal surface density that are not resolved by gravimetric porosity alone. Materials with more complex and finer pore networks, as determined by micro-CT analysis, tend to exhibit increased stress concentration sites and reduced mechanical performance (series LF20 and LF20-W), as highly tortuous pore geometries disrupt load transfer and promote localized stress amplification under compressive loading [48]. In contrast, simpler pore structures generally correlate with improved mechanical behavior.

Total porosity is commonly used as a primary descriptor of mechanical performance in cementitious materials, the present results demonstrate that pore morphology and internal surface complexity play an equally important role, representing the density of the internal pore surface and are conceptually equivalent to pore-specific surface area widely used in cement science. Materials with higher PSA/MV values exhibited more complex, finer pore networks, associated with increased stress concentration sites and reduced load-transfer efficiency. Conversely, the material with the lowest PSA/MV demonstrated superior compressive strength, indicating the possibility that carbonation-driven densification not only reduces pore volume but also smooths and partially closes the fine pore network [49]. These observations confirm that strength development in carbonated alkali-activated systems is governed by pore-network topology and internal surface characteristics leading to significant improvement of compressive strength in carbonated cured series.

The formation of vaterite and aragonite in addition to calcite indicates rapid carbonation under conditions of high CO_2 availability, with subsequent polymorphic transformations contributing to progressive microstructural refinement. Metastable calcium carbonate polymorphs such as vaterite and aragonite are typically favored during early carbonation stages due to kinetic effects and high supersaturation, but gradually transform into thermodynamically stable calcite as carbonation proceeds[50].

These mineralogical transformations yield a denser and mechanically more stable microstructure, consistent with the substantial increase in compressive strength and the marked reduction in water absorption observed for the LF20-C samples. Carbonation leads to the consumption of calcium-bearing hydrates and non-hydraulic γ-belite, replacing them with chemically stable carbonate phases that reinforce the load-bearing skeleton. At the same time, the observed decrease in absolute density following carbonation can be rationalized by the decalcification of calcium silicate and aluminate hydrates and the carbonation of γ-belite, processes that liberate calcium to form $CaCO_3$ while leaving behind amorphous SiO_2 or silica–alumina gels, which possess lower absolute density than the original crystalline or semi-crystalline calcium-containing phases [51]. The results indicate that carbonation acts simultaneously as a microstructural densification mechanism and a phase-transformation pathway, confirming its relevance as a post-treatment strategy for alkali-activated materials targeting both carbon sequestration and mechanical enhancement.

4.2. Carbonation of γ-Belite and Role of High Alkalinity

A key finding of the present study is the complete carbonation of γ-belite in the LF20-C series without preceding hydration. Recent work by Chen et al. systematically demonstrated that elevated pH environments markedly enhance the carbonation degree, kinetics, and strength development of γ-C_2S pastes under CO_2 curing [52]. In their study, γ-belite exposed to strongly alkaline conditions (pH >12) exhibited accelerated Ca^{2+} migration, increased carbonate precipitation, and a dense microstructure dominated by calcite, achieving compressive strengths exceeding 45 MPa after CO_2 curing. This behavior is similar to observed in the present study for series LF20-C, which reached compressive strengths above 48 MPa, despite the absence of hydraulic activation of γ-belite. The high alkalinity was generated by the dissolution of free lime, alkali sulfates, and alkali chlorides from CKD. Such conditions are expected to promote high concentrations of CO_3^{2-} relative to HCO_3^- in the pore solution, favoring direct precipitation of $CaCO_3$ according to the reaction pathway $Ca^{2+} + CO_3^{2-} \rightarrow CaCO_3$, identified as dominant at pH ≥ 12 in γ-belite systems [52]. In contrast, when alkalinity is insufficient, ladle furnace slag exhibits limited reactivity and resists carbonation [25].

The presence of γ-belite plays an beneficial role in CO_2 curing when embedded in a highly alkaline alkali-activated matrix. The results demonstrates that high alkalinity can be exploited to activate the carbonation potential of otherwise hydraulically inactive phases. This finding reinforces the suitability of LFS–CA–CKD binders for carbonation-based curing strategies aimed at simultaneous strength enhancement and CO_2 sequestration. However, another hydraulically inactive phase, periclase (MgO), did not exhibit significant reactivity under the investigated curing conditions.

4.3. Influence of Chloride and Sulfate Contents and Implications for Application Fields

The elevated chloride and sulfate contents inherent to the LFS–CA–CKD system exert an influence on potential applications. Sulfate supplied mainly by coal ash stabilizes calcium in AFt and

AFm phases under non-carbonated conditions, while chloride originating predominantly from CKD is incorporated into chloride-bearing AFm phases such as hydrocalumite. As a result, part of the calcium is chemically immobilized in sulfate- and chloride-containing phases, reducing its availability for carbonation and altering the evolution of hydration products. Although the AFm phase hydrocalumite is capable of binding chloride ions, leaching studies on biomass-ash-based alkali-activated materials have shown that substantial amounts of chloride, sulfate, and potassium remain mobile and can be released [53].

However, from an application standpoint, the presence of chlorides renders the investigated binder system unsuitable for use in steel-reinforced concrete due to the risk of corrosion. However, this limitation does not preclude a wide range of non-reinforced applications, including masonry blocks, paving elements, lightweight panels, backfilling materials, and radiation-shielding or encapsulation products [54]. In such applications, the high early strength achieved through carbonation and the reduced water absorption of LF20-C are particularly advantageous.

Potential leaching of alkalis, chlorides, and sulfates remains an important consideration, especially for environmental or structural applications. Although carbonation generally reduces permeability and immobilizes calcium in stable carbonate phases, the mobility of alkali ions and residual anions was not addressed in the present study. Consequently, leaching behavior should be evaluated in future work to fully assess environmental compatibility.

4.4. Carbonation Regime and Relevance to Practical Curing Conditions

It is important to distinguish the carbonation regime employed in this study from more aggressive carbonation approaches reported in the literature. Previous studies have demonstrated rapid strength gain using pressurized CO_2, elevated temperatures, or industrial exhaust gases, such as cement kiln bypass or flue gas streams [55–57]. While these methods can significantly accelerate carbonation kinetics, they often induce steep concentration gradients and near-surface densification, which may limit CO_2 penetration depth.

In contrast, the carbonation conditions applied here—ambient pressure, moderate relative humidity, and gaseous CO_2—are closer to natural carbonation environments. The phenolphthalein test confirmed complete carbonation across the specimen cross-section, indicating that the selected regime enables uniform CO_2 ingress and bulk phase transformation rather than surface-limited reactions. This distinction is particularly relevant for thick or massive elements, where homogeneous carbonation is required to achieve consistent mechanical performance.

Therefore, although the applied CO_2 concentration exceeds atmospheric levels, the overall curing concept represents a transitional approach between natural and accelerated carbonation. This makes the findings directly relevant to practical curing strategies that aim to balance processing simplicity, material performance, and scalability

4.5. Overall Implications and Limitations

The results demonstrate that CO_2 curing is an effective post-treatment strategy for Ca-rich alkali-activated binders derived entirely from industrial residues. Carbonation transforms both hydration products and non-hydraulic phases, including γ-belite, into mechanically beneficial carbonate phases, leading to substantial strength enhancement and pronounced microstructural densification.

At the same time, not all crystalline phases present in the system actively participate in carbonation or strength development. Periclase (MgO) was detected as a largely unreacted phase under all curing regimes, including the carbonated LF20-C series. This behavior indicates that the MgO present in the ladle furnace slag exhibits low reactivity under both hydration and carbonation conditions and is most likely predominantly dead-burned [58]. Similar behavior has been reported for steelmaking slags, where high-temperature formation results in coarse, well-crystallized periclase with limited hydration and carbonation potential [59]. However, the long-term stability of residual periclase under service conditions cannot be fully excluded, particularly in environments involving prolonged moisture exposure, where delayed MgO hydration could induce volumetric instability.

No evidence of such effects was observed within the investigated curing period, including 28 days of water curing for series LF20-W. Nevertheless, long-term dimensional stability should be addressed in future durability-oriented studies, as well as leaching behavior, and performance under cyclic environmental exposure

Despite these limitations, the present work provides clear mechanistic evidence that controlled carbonation can be exploited to activate otherwise inert or weakly reactive phases in waste-derived alkali-activated systems. This approach opens viable pathways toward low-clinker, non-reinforced construction materials that combine improved mechanical performance with intrinsic CO_2 sequestration potential.

5. Conclusions

This study demonstrates that carbonation curing provides a clear dual benefit for LFS–CA–CKD alkali-activated binders: effective CO_2 uptake and a near-doubling of compressive strength. Accelerated carbonation resulted in complete carbonation throughout the specimens cross-section. Calcium-bearing hydrates and non-hydraulic γ-belite were transformed into $CaCO_3$ polymorphs (calcite, vaterite and aragonite), resulting in pronounced matrix densification, significant reduction in water absorption, refinement of the pore network in terms of reduced porosity, simplified pore morphology and decreased internal surface complexity.

These findings confirm carbonation curing as an effective post-treatment strategy for waste-derived, Ca-rich alkali-activated materials based on industrial residues, enabling simultaneous mechanical improvement and CO_2 sequestration.

Author Contributions: "Conceptualization, A.N.; methodology, A.N.; software, A.N., N.P., M.R., I.G. and A.K.; validation, A.N., N.P., M.R., I.G. and A.K.; formal analysis, A.N., N.P., M.R., I.G. and A.K.; investigation, A.N., N.P., M.R., I.G. and A.K.; resources, A.N., N.P., M.R., I.G. and A.K.; data curation, A.N., N.P., M.R., I.G. and A.K.; writing—original draft preparation, A.N.; writing—review and editing, A.N., N.P., M.R., I.G. and A.K.; visualization, A.N., N.P., M.R. and I.G.; supervision, A.N.; project administration, A.K.; funding acquisition, A.K. All authors have read and agreed to the published version of the manuscript.".

Funding: This research was financially supported by National Recovery and Resilience Plan (NRRP) project BG-RRP-2.017-0024-C01 "Using inorganic technogenic wastes in production of new construction materials with improved properties (WasteNewMat)".

Acknowledgments: We would like to express our gratitude to programme "Research, Innovation and Digitalisation for Smart Transformation" 2021-2027, funded by the European Union, Project BG16RFPR002-1.014-0007, Center for Competence "PERIMED-2" for technical support (Powder XRD). The authors gratefully acknowledge Aeiforos Bulgaria S.A. for supplying the ladle furnace slag used in this study, and Heidelberg Materials Devnya JSC for providing the cement kiln dust. Their support in the provision of raw materials is sincerely appreciated.

Conflicts of Interest: The authors declare no conflicts of interest. The funders had no role in the design of the study; in the collection, analyses, or interpretation of data; in the writing of the manuscript; or in the decision to publish the results.

Abbreviations

The following abbreviations are used in this manuscript:

AAM	Alkali-Activated Materials
LFS	Ladle Furnace Slag
CKD	Cement Kiln Dust
CA	Coal Ash

References

1. UN. Global Status Report for Buildings and Construction 2024/25: Not Just Another Brick in the Wall. **2025**.
2. Antunes, M.; Santos, R.L.; Pereira, J.; Rocha, P.; Horta, R.B.; Colaço, R. Alternative clinker technologies for reducing carbon emissions in cement industry: a critical review. *Materials* **2021**, *15*, 209.
3. Ahmad, M.R.; Fernández-Jiménez, A.; Chen, B.; Leng, Z.; Dai, J.-G. Low-carbon cementitious materials: Scale-up potential, environmental impact and barriers. *Available at SSRN 4947974* **2025**.
4. Naqvi, S.M.O.; Raza, M.D.; Haider, S.H. Carbon-Neutral Concrete: A Review on Carbon Capture, Storage, and Utilization Technologies. *Journal of Advanced Concrete Technology* **2025**, *23*, 531-545.
5. Boakye, K.; Winters, D.; Oguntola, O.; Fenton, K.; Simske, S. A review of strategies to achieve net zero targets in the cement and concrete sectors. *Reducing Carbon Footprint in Different Sectors for Sustainability* **2024**.
6. Liao, W.; Cai, K.; Huang, Y.; Zhang, N.; Deng, G.; Javed, M.H.; Ma, H. CO2 Utilization in Cement and Concrete. *Industrial Decarbonization* **2025**, 287-322.
7. Winnefeld, F.; Leemann, A.; German, A.; Lothenbach, B. CO2 storage in cement and concrete by mineral carbonation. *Current Opinion in Green and Sustainable Chemistry* **2022**, *38*, 100672.
8. Shi, M.; Ling, T.-C.; Gan, B.; Guo, M.-Z. Turning concrete waste powder into carbonated artificial aggregates. *Construction and Building Materials* **2019**, *199*, 178-184.
9. Zhang, J.; Shi, C.; Li, Y.; Pan, X.; Poon, C.-S.; Xie, Z. Performance enhancement of recycled concrete aggregates through carbonation. *Journal of Materials in Civil Engineering* **2015**, *27*, 04015029.
10. Zhang, Z.; Angst, U.; Troian, V.; Guo, B.; Zeng, Q. Durability performance of concrete incorporating carbonated recycled coarse aggregates: a review. *npj Materials Sustainability* **2025**, *3*, 27.
11. Ghouleh, Z.; Guthrie, R.I.; Shao, Y. Production of carbonate aggregates using steel slag and carbon dioxide for carbon-negative concrete. *Journal of CO2 Utilization* **2017**, *18*, 125-138.
12. Saridhe, S.P.; Hareesh, M.; Selvaraj, T. Role of olivine aggregate in lime and cement mortars for the sequestration of atmospheric CO2. *Materials and Technology* **2023**, *57*, 135–140-135–140.
13. Huntzinger, D.N.; Gierke, J.S.; Kawatra, S.K.; Eisele, T.C.; Sutter, L.L. Carbon dioxide sequestration in cement kiln dust through mineral carbonation. *Environmental science & technology* **2009**, *43*, 1986-1992.
14. Nikolov, A.; Kostov-Kytin, V.; Tarassov, M.; Tsvetanova, L.; Lazarova, H.; Tasheva, T. Products of carbonation of cement kiln dust. *Review of the Bulgarian Geological Society* **2024**, *85*, 163-166.
15. Vassilev, S.V.; Vassileva, C.G.; Petrova, N.L. Mineral carbonation of biomass ashes in relation to their CO2 capture and storage potential. *ACS omega* **2021**, *6*, 14598-14611.
16. Hanifa, M.; Sharma, U.; Thapliyal, P.; Singh, L. Studies on Sustainable Concrete Incorporating Carbonated Aggregates Developed from Industrial Waste. *Journal of Materials in Civil Engineering* **2026**, *38*, 04025568.
17. Thonemann, N.; Zacharopoulos, L.; Fromme, F.; Nühlen, J. Environmental impacts of carbon capture and utilization by mineral carbonation: A systematic literature review and meta life cycle assessment. *Journal of Cleaner Production* **2022**, *332*, 130067.
18. Pan, S.-Y.; Chiang, P.-C.; Pan, W.; Kim, H. Advances in state-of-art valorization technologies for captured CO2 toward sustainable carbon cycle. *Critical reviews in environmental science and technology* **2018**, *48*, 471-534.
19. Provis, J.L. Alkali-activated materials. *Cement and concrete research* **2018**, *114*, 40-48.
20. Mehta, A.; Siddique, R. An overview of geopolymers derived from industrial by-products. *Construction and building materials* **2016**, *127*, 183-198.
21. Zaharaki, D.; Galetakis, M.; Komnitsas, K. Valorization of construction and demolition (C&D) and industrial wastes through alkali activation. *Construction and building Materials* **2016**, *121*, 686-693.
22. Molahid, V.L.M.; Mohd Kusin, F.; Syed Hasan, S.N.M.; Ramli, N.A.A.; Abdullah, A.M. CO2 sequestration through mineral carbonation: effect of different parameters on carbonation of Fe-rich mine waste materials. *Processes* **2022**, *10*, 432.
23. Yi, Y.-R.; Lin, Y.; Du, Y.-C.; Bai, S.-q.; Ma, Z.-l.; Chen, Y.-g. Accelerated carbonation of ladle furnace slag and characterization of its mineral phase. *Construction and Building Materials* **2021**, *276*, 122235.
24. Xu, B.; Yi, Y. Treatment of ladle furnace slag by carbonation: Carbon dioxide sequestration, heavy metal immobilization, and strength enhancement. *Chemosphere* **2022**, *287*, 132274.

25. Kaddah, F.; Abdelgawad, A.H.; Dumée, L.F.; Al Amoodi, N.; Barsoum, I.; Alhajaj, A. Accelerated carbonation of ladle furnace slag: A dual approach to CO2 utilization and waste valorization in sustainable cement applications. *Journal of CO2 Utilization* **2025**, *102*, 103267.
26. Nikolov, A.; Jordanov, N.B.; Djobov, I.; Karamanov, A. Toward Zero-Carbon Concrete: Alkali Activation of Ladle Furnace Slag Using Cement Kiln Dust. *Buildings* **2025**, *15*, 4402.
27. Djobov, I.; Karamanova, E.; Avdeev, G.; Karamanov, A. CHARACTERIZATION OF CLAYS FROM "MINES MARITSA IZTOK" AS RAW MATERIALS FOR CERAMIC INDUSTRY. *Journal of Chemical Technology and Metallurgy* **2024**, *59*, 1331-1340.
28. Nikolov, A.; Kostov-Kytin, V.; Tarassov, M.; Tsvetanova, L.; Jordanov, N.B.; Karamanova, E.; Rostovsky, I. Characterization of cement kiln dust from Bulgarian cement plants. *Journal of Chemical Technology and Metallurgy (JCTM)* **2025**, *60*, 455-463.
29. Pyatina, T.; Sugama, T. Aluminum-Rich Cements for High Temperature Geothermal Wells. In Proceedings of the Proceedings of the 49th Workshop Geothermal Reservoir Engineering, Stanford, CA, USA, 2024; pp. 12-14.
30. Pyatina, T.; Sugama, T. Role of tartaric acid in chemical, mechanical and self-healing behaviors of a calcium-aluminate cement blend with fly ash f under steam and alkali carbonate environments at 270 c. *Materials* **2017**, *10*, 342.
31. Grishchenko, R.O.; Emelina, A.L.; Makarov, P.Y. Thermodynamic properties and thermal behavior of Friedel's salt. *Thermochimica acta* **2013**, *570*, 74-79.
32. Rossi, T.M.; Campos, J.C.; Souza, M.M. Synthesis and characterization of hydrocalumite: influence of aging conditions on the structure, textural properties, thermal stability, and basicity. *Clays and Clay Minerals* **2020**, *68*, 273-286.
33. Jiménez, A.; Rives, V.; Vicente, M.A. Thermal study of the hydrocalumite–katoite–calcite system. *Thermochimica Acta* **2022**, *713*, 179242.
34. Guimaraes, D.; de A. Oliveira, V.; Leao, V.A. Kinetic and thermal decomposition of ettringite synthesized from aqueous solutions. *Journal of Thermal Analysis and Calorimetry* **2016**, *124*, 1679-1689.
35. Chakoumakos, B.C.; Pracheil, B.M.; Koenigs, R.P.; Bruch, R.M.; Feygenson, M. Empirically testing vaterite structural models using neutron diffraction and thermal analysis. *Scientific Reports* **2016**, *6*, 36799.
36. Popescu, M.-A.; Isopescu, R.; Matei, C.; Fagarasan, G.; Plesu, V. Thermal decomposition of calcium carbonate polymorphs precipitated in the presence of ammonia and alkylamines. *Advanced Powder Technology* **2014**, *25*, 500-507.
37. Földvári, M. *Handbook of thermogravimetric system of minerals and its use in geological practice*; Geological Institute of Hungary Budapest: 2011; Volume 213.
38. Chattaraj, B.; Dutta, S.; Iyengar, M. Studies on the thermal decomposition of calcium carbonate in the presence of alkali salts (Na2CO3, K2CO3 and NaCl). *Journal of thermal analysis* **1973**, *5*, 43-49.
39. Deb, S.; Manghnani, M.; Ross, K.; Livingston, R.; Monteiro, P. Raman scattering and X-ray diffraction study of the thermal decomposition of an ettringite-group crystal. *Physics and chemistry of minerals* **2003**, *30*, 31-38.
40. Tian, J.; Guo, Q. Thermal decomposition of hydrocalumite over a temperature range of 400–1500 C and its structure reconstruction in water. *Journal of Chemistry* **2014**, *2014*, 454098.
41. Trezza, M.; Lavat, A. Analysis of the system 3CaO· Al2O3–CaSO4· 2H2O–CaCO3–H2O by FT-IR spectroscopy. *Cement and Concrete Research* **2001**, *31*, 869-872.
42. Wu, B.; Ye, G. Study of carbonation rate of synthetic CSH by XRD, NMR and FTIR. *Heron* **2019**, *64*, 21-38.
43. González-Gómez, M.A.; Belderbos, S.; Yañez-Vilar, S.; Piñeiro, Y.; Cleeren, F.; Bormans, G.; Deroose, C.M.; Gsell, W.; Himmelreich, U.; Rivas, J. Development of superparamagnetic nanoparticles coated with polyacrylic acid and aluminum hydroxide as an efficient contrast agent for multimodal imaging. *Nanomaterials* **2019**, *9*, 1626.
44. Puertas, F.; Palacios, M.; Vázquez, T. Carbonation process of alkali-activated slag mortars. *Journal of materials science* **2006**, *41*, 3071-3082.
45. Hwalla, J.; Al-Mazrouei, M.; Al-Karbi, K.; Al-Hebsi, A.; Al-Ameri, M.; Al-Hadrami, F.; El-Hassan, H. Performance of alkali-activated slag concrete masonry blocks subjected to accelerated carbonation curing. *Sustainability* **2023**, *15*, 14291.

46. Jun, Y.; Han, S.H.; Kim, J.H. Early-age strength of CO2 cured alkali-activated blast furnace slag pastes. *Construction and Building Materials* **2021**, *288*, 123075.
47. Yoon, J.; Kim, H.; Sim, S.-H.; Pyo, S. Characterization of porous cementitious materials using microscopic image processing and X-ray CT analysis. *Materials* **2020**, *13*, 3105.
48. Chung, S.-Y.; Lehmann, C.; Abd Elrahman, M.; Stephan, D. Pore characteristics and their effects on the material properties of foamed concrete evaluated using micro-CT images and numerical approaches. *Applied Sciences* **2017**, *7*, 550.
49. Abousnina, R.; Aljuaydi, F.; Benabed, B.; Almabrok, M.H.; Vimonsatit, V. A State-of-the-Art Review on the Influence of Porosity on the Compressive Strength of Porous Concrete for Infrastructure Applications. *Buildings* **2025**, *15*, 2311.
50. Bertos, M.F.; Simons, S.; Hills, C.; Carey, P. A review of accelerated carbonation technology in the treatment of cement-based materials and sequestration of CO2. *Journal of hazardous materials* **2004**, *112*, 193-205.
51. Adekunle, S.K. Carbon sequestration potential of cement kiln dust: mechanisms, methodologies, and applications. *Journal of Cleaner Production* **2024**, *446*, 141283.
52. Chen, Z.; Zhang, N.; Chu, S. Role of alkalinity in CO2 sequestration of γ-belite. *Construction and Building Materials* **2024**, *432*, 136508.
53. Nikolov, A.; Kostov, V.; Petrova, N.; Tsvetanova, L.; Vassilev, S.V.; Titorenkova, R. Sunflower Shells Biomass Fly Ash as Alternative Alkali Activator for One-Part Cement Based on Ladle Slag. *Ceramics* **2025**, *8*, 79.
54. Wu, L.; Li, H.; Mei, H.; Rao, L.; Wang, H.; Lv, N. Generation, utilization, and environmental impact of ladle furnace slag: A minor review. *Science of The Total Environment* **2023**, *895*, 165070.
55. Biava, G.; Zacco, A.; Zanoletti, A.; Sorrentino, G.P.; Capone, C.; Princigallo, A.; Depero, L.E.; Bontempi, E. Accelerated direct carbonation of steel slag and cement kiln dust: an industrial symbiosis strategy applied in the Bergamo–Brescia area. *Materials* **2023**, *16*, 4055.
56. Abdel-Ghani, N.T.; El-Sayed, H.A.; El-Habak, A.A. Utilization of by-pass cement kiln dust and air-cooled blast-furnace steel slag in the production of some "green" cement products. *HBRC journal* **2018**, *14*, 408-414.
57. Zhang, S.; Ghouleh, Z.; Liu, J.; Shao, Y. Converting ladle slag into high-strength cementing material by flue gas carbonation at different temperatures. *Resources, Conservation and Recycling* **2021**, *174*, 105819.
58. Landy, R.A. Magnesia refractories. *Mechanical Engineering-New York and Basel-Marcel Dekker Then Crc Press/Taylor and Francis* **2004**, *178*, 109.
59. Wang, S.; Wang, M.; Liu, F.; Song, Q.; Deng, Y.; Ye, W.; Ni, J.; Si, X.; Wang, C. A review on the carbonation of steel slag: properties, mechanism, and application. *Materials* **2024**, *17*, 2066.